Thermoplasmonic In Situ Fabrication of Nanohybrid Electrocatalysts over Gas Diffusion Electrodes for Enhanced H_2O_2 Electrosynthesis

Yu Zhang, Luca Mascaretti, Michele Melchionna, Olivier Henrotte, Štepan Kment, Paolo Fornasiero, and Alberto Naldoni*

Cite This: *ACS Catal.* 2023, 13, 10205−10216

Read Online

ACCESS | Metrics & More | Article Recommendations | Supporting Information

ABSTRACT: Large-scale development of electrochemical cells is currently hindered by the lack of Earth-abundant electrocatalysts with high catalytic activity, product selectivity, and interfacial mass transfer. Herein, we developed an electrocatalyst fabrication approach which responds to these requirements by irradiating plasmonic titanium nitride (TiN) nanocubes self-assembled on a carbon gas diffusion layer in the presence of polymeric binders. The localized heating produced upon illumination creates unique conditions for the formation of TiN/F-doped carbon hybrids that show up to nearly 20 times the activity of the pristine electrodes. In alkaline conditions, they exhibit enhanced stability, a maximum H_2O_2 selectivity of 90%, and achieve a H_2O_2 productivity of 207 mmol g_{TiN}^{-1} h^{-1} at 0.2 V vs RHE. A detailed electrochemical investigation with different electrode arrangements demonstrated the key role of nanocomposite formation to achieve high currents. In particular, an increased TiO_xN_y surface content promoted a higher H_2O_2 selectivity, and fluorinated nanocarbons imparted good stability to the electrodes due to their superhydrophobic properties.

KEYWORDS: *thermoplasmonics, oxygen reduction reaction, plasmonics, titanium nitride, nanohybrids, electrocatalysis*
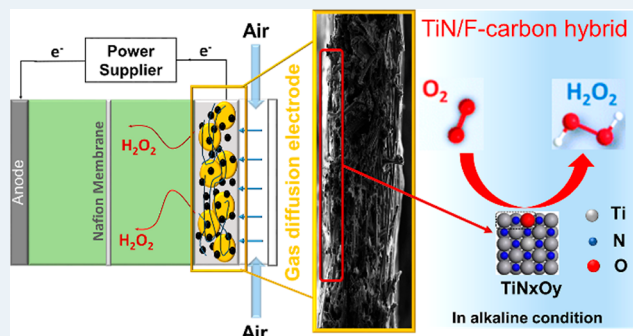
INTRODUCTION

Increasing concerns about global warming have prompted worldwide efforts in developing innovative energy storage technologies. Electrochemistry plays a crucial role in such a transition to sustainable processes as mean of either storing electrical energy in chemical bonds generating fuels, such as in water splitting,[1,2] CO_2 reduction,[3,4] hydrogen peroxide (H_2O_2) production,[5,6] or generating electrical energy by consuming such fuels, such as in fuel cells[7,8] or in metal-air batteries.[9] Among these processes, the oxygen reduction reaction (ORR) is central for many technologies. It may occur according to a four-electron pathway ($O_2 + 4H^+ + 4e^- \rightarrow 2H_2O$) at the cathodic side in both fuel cells and metal-air batteries, respectively.[10] On the other hand, the ORR can also proceed along a two-electron pathway, leading to hydrogen peroxide ($O_2 + 2H^+ + 2e^- \rightarrow H_2O_2$).[11] Although H_2O_2 is an undesired side product in fuel cells,[12] its synthesis through electrochemical approach has recently attracted considerable attention due to the possibility for decentralized H_2O_2 production.[13−18]

While state-of-the-art cathodes for the ORR are based on Pt nanoparticles (NPs) loaded on carbon supports (Pt/C),[19] alternative Pt-free electrodes based on doped carbon nanostructures[20−23] or on transition-metal nitrides (TMNs) have been considered[24−27] due to their high ORR activity maintaining low cost. Heteroatom-doped carbon catalysts, particularly in the nanostructured form, have been the subject of wide interest in H_2O_2 electrochemical synthesis. In this case, the presence of atoms with different electronegativity inserted within the graphitic carbon lattice may tune the charge distribution on the carbon atoms adjacent to the heteroatom. The resulting polarization favors optimum O_2 adsorption, triggering the selective reduction pathway. While nitrogen is the most investigated heteroatom, various non-metal elements have been screened and their effect evaluated in the realm of $2e^-$ ORR, including fluorine.[28,29] Notably, F-doped carbons show a high positive charge over the carbon framework due to the highest electronegativity of fluorine atoms, which show great potential for ORR,[30] especially facilitating the desorption of the *OOH intermediate.[31] Besides doped carbon, TMNs are well-suited as electrocatalysts due to their exceptional electrical conductivity, chemical stability, wear resistance, and mechanical robustness.[32−34] The limited performance of TMNs compared to commercial Pt/C can be improved through doping[35,36] or by

partial oxidation, leading to oxynitride phases.[27,37−42] Furthermore, a fully or partially oxidized surface layer can increase the selectivity toward the 2e⁻ ORR over the 4e⁻ ORR, as shown in the case of titanium nitride/oxynitride (TiN/TiO_xN_y) electrocatalysts.[38,40,43,44]

Apart from the field of electrochemistry, the refractory nature of TMNs coupled with their similar optical properties to Au has led to their implementation as alternative plasmonic materials to substitute coinage metals, especially in the so-called field of thermoplasmonics, which makes use of the photothermal heat generated after surface plasmon dissipation and hot carrier thermalization.[32,33,45−47] The photothermal properties of TMNs have been shown to be beneficial in promoting chemical transformations, in material synthesis,[48−51] solar desalination,[47,52] catalysis,[53−55] and as nanosources of heat.[47] In particular, electromagnetic hotspots in plasmonic materials enable the generation of significant local heating with characteristic ultrafast heating/cooling rates of ∼25 °C s⁻¹ for TiN nanostructures, thus producing unique conditions for nanomaterial synthesis.[45]

Gas diffusion electrodes (GDEs) are chosen as they represent a benchmark to industrially scaling electrochemical processes by allowing substantially higher reaction currents compared to traditional electrode configurations.[56,57] However, GDEs tend to lose their hydrophobicity during longtime electrolysis, leading to the flooding of the electrodes and, consequently, a decrease in O_2 mass transport and performance over time. In order to overcome these limitations, GDE functionalization to generate engineered reaction microenvironment[58] and superhydrophobic surfaces,[59,60] which ensure stable solid−gas−liquid triple phase interfaces, has been proposed as effective strategies. For example, surface fluorination is an efficient approach to tuning surface wettability.[61−65] In particular, Nafion polymer,[66] polytetrafluoroethylene (PTFE),[64] and others fluorinated organic binders[30] have been proposed as precursors to synthesize F-doped nanocarbons. However, the high cost of Nafion raises questions about the scalability of the approach, while PTFE can be a more viable solution as demonstrated for electrocatalytic CO_2 reduction.[67] Thus, an efficient and more convenient strategy for the synthesis of F-doped nanocarbons to fabricate stable GDEs is still a challenge.

Here, we present a thermoplasmonic synthesis approach, leading to TiN/F-doped carbon hybrid cathodes for the ORR with enhanced activity and selectivity toward H_2O_2 electrosynthesis. In such nanohybrids, each material provided functional properties to boost the performance of the cathodes that were directly assembled as GDEs using natural air to feed the ORR. In particular, plasmonic TiN in the form of nanocubes was chosen as an electrochemically active phase and to provide plasmonic local heating upon irradiation. Carbon fiber was chosen as a catalyst backing layer to form GDE to enhance O_2 mass transport and improve the electrochemical activity. Surface fluorination was then achieved through the decomposition of F-containing organic binders upon irradiation to both induce enhanced activity and higher hydrophobicity to the hybrid electrodes, where the latter is paramount to avoid flooding of GDEs and ensure a constant supply of O_2.[59,60,64] PTFE was chosen as a low cost fluorinated alternative to Nafion, whose final nanohybrid electrocatalyst performance were compared with a non-fluorinated binder. The unique conditions created during thermoplasmonic synthesis led to the TiN surface enrichment in $Ti^{(III)}O_xN_y$ species, which favored the 2e⁻ ORR over the 4e⁻ ORR, and the formation of F-doped nanocarbons,

which ensured a stable three-phase interface during the electrochemical reactions. The so-realized hybrid TiN/F-carbon GDE exhibited an ORR current of ∼25 mA cm⁻² at 0.1 V vs RHE and a maximum faradaic efficiency (FE) toward H_2O_2 production of ∼75% at 0.5 V vs RHE. This work provides a new paradigm to enhance the electrochemical activity of nanohybrids toward H_2O_2 and offers a scalable and universal plasmon-assisted fabrication route toward in situ functionalization of GDEs, which could be easily implemented into electrochemical cells for the synthesis of a wide variety of commodity chemicals.

■ EXPERIMENTAL SECTION

Materials and Chemicals. Toray carbon paper (TGP-H-60) without PTFE treatment was purchased from Alfa Aesar. Sulfuric acid (95−98% H_2SO_4), polytetrafluoroethylene (PTFE) 60 wt % dispersion in water, polyvinyl alcohol (PVA) powder M_w = 146,000−186,000, KOH pellet, and Nafion perfluorinated resin solution (5 wt %) were purchased from Sigma-Aldrich. 30 wt % H_2O_2 was purchased from Lanchner. Ethanol (absolute) was purchased from Penta. Commercial TiN nanocubes were obtained from PlasmaChem GmbH (average size ∼ 50 nm). All aqueous solutions were prepared with ultrapure water (18 MΩ cm⁻¹). All the chemicals and materials were used without further treatment.

Electrode Preparation. The TiN/binder ink was prepared by adding 10 mg of TiN and 20 μL of 5 wt % binder solution Nafion, PTFE, and PVA solution to ethanol to reach a concentration of 10 mg mL⁻¹, then sonicating for 30 min. 50 μL of the precursor ink was drop-cast on each side over a 5 × 27 mm Toray carbon paper and heated at 70 °C by using a heating plate to enhance the solvent evaporation. The same procedure was applied for the fabrication of self-supported GDEs, enlarging the coated area to 7 × 27 mm and drop-casting on each side of the Toray paper 70 μL of the precursor ink. The electrodes were then put into a 50 mL Schlenk tube glass, which was evacuated with a vacuum pump (EDWARDS model E2M1.5) for 30 min. Then, the sample was irradiated from one side by means of solar-simulated light provided by a 1000 W solar simulator (Sciencetech A4 Lightline C250) equipped with a xenon short arc lamp (Osram XBO 1000W/HS OFR). Two lenses (i.e., a fused silica plano-convex lens, Thorlabs LA4984, and a Fresnel lens, Thorlabs FRP251) were employed to focus the light beam down to a circular spot of 1 cm diameter with an average intensity of 1.5 W cm⁻² (i.e., 15 Suns), which was measured with a thermopile detector (Standa 11UP19K-30 H-H5) prior to every experiments. The scheme of the set-up employed for the electrode synthesis is illustrated in Figure S1.

Characterization. Fourier-transform infrared (FTIR) spectroscopy measurements were performed with a vacuum Vertex 80v spectrometer in the reflectance mode in the spectral range 1330−25,000 nm at room temperature. The reflectance spectra were converted to absorptance according to the formula $A_{FTIR}(\lambda, T_0) = 1 - R_{FTIR}(\lambda, T_0)$ and, in turn, the spectral emissivity was retrieved by Kirchhoff's law of thermal radiation: $\varepsilon_\lambda(\lambda, T_0) = A_{FTIR}(\lambda, T_0)$.

The Raman spectra were measured on a DXR Raman spectrometer (Thermo Scientific, USA) with a laser operating at 633 nm. The sample was deposited on a silicon wafer (1 × 1 cm), and an excitation laser was focused on its surface. The laser power on the sample was set to 2 mW, and the exposition time was 2 s. Each measured Raman spectrum was an average of 64 experimental scans. The Raman spectra were processed using control software (Omnic, version 8, Thermo Scientific, USA).

X-ray diffraction (XRD) patterns were recorded at room temperature with an Empyrean (PANalytical, The Netherlands) diffractometer in the grazing-incidence mode (GIXRD) geometry, Co Kα radiation (40 kV, 30 mA, λ = 0.1789 nm) equipped with a PIXcel3D detector, and programmable divergence and diffracted beam anti-scatter slits. The samples were placed on a zero-background Si slide. The measurement range was 2θ: 20−80°, with a step size of 0.026°. The GIXRD experiments were performed using an incidence angle of 15°.

X-ray photoelectron spectroscopy (XPS) analysis were performed on a PHI 5000 VersaProbe II XPS system (Physical Electronics) with a monochromatic Al Kα source (15 kV, 50 W) and a photon energy of 1486.7 eV. High-resolution (HR) spectra were scaled using the adventitious carbon peak as a reference at 284.8 eV and fitted with MultiPak (Ulvac-PHI, Inc.) software.

The low-resolution imaging of the catalyst morphology was obtained with a transmission electron microscope (TEM) JEOL equipped with a LaB$_6$ emission gun and operating at 160 kV. HR micrographs and STEM elemental mapping were acquired using a FEI Titan HR-TEM microscope equipped with X-FEG electron gun operating at 80 kV.

Scanning electron microscopy (SEM) was used to examine the morphology of the GDEs before and after irradiation. The measurements were carried out with a Scios 2 DualBeam microscope (ultra-HRSEM/FIB, Thermo Fisher Scientific) with an accelerating voltage of 5 kV.

The UV−vis absorption spectra were acquired with a Specord250 Plus spectrometer equipped with an integrating sphere (Analytik Jena GmbH).

The contact angle measurements were carried out using the sessile drop method. A water droplet of 4 μL was placed over the film electrodes, and the image of the droplet was taken by a HR camera. The contact angle was then determined by Image software.

Electrochemical Measurements. Linear sweep voltammetry (LSV) measurements for Toray paper-based electrodes were carried out in a homemade three-electrode system with a bipotentiostat (Autolab Instruments). The three electrode arrangement consisted of a Pt sheet as the counter electrode (CE), Ag/AgCl (3 M) as the reference electrode (RE), and a working electrode (WE) made by the investigated samples with active geometric area of 0.5 × 1.5 cm on both sides. After 30 min bubbling of O$_2$ gas, the WE was inserted into the electrolyte. The testing was conducted after WE was placed into the electrolyte, and cyclic voltammetry (CV) and LSV scans were carried out. The O$_2$ was continuously bubbled during the electrochemistry measurements.

Bulk H$_2$O$_2$ production with Toray paper-based electrodes was carried out in a custom-made two-compartment H-cell with Nafion 117 membrane as the separator. Both the cathode and anode compartment were filled with 30 mL of 0.1 M KOH (pH = 13). H$_2$O$_2$ production was conducted by chronoamperometry at selected potential with bubbling O$_2$ into the cathodic part and magnetic stirring at 900 rpm. The liquid collected at a certain time from the cathodic compartment was analyzed using a commercial test KIT (Merck KGaA, Germany) to quantify H$_2$O$_2$. In detail, 2 mL of the electrolyte was taken from the cathodic compartment, then diluted with 8 mL of H$_2$O, and neutralized by 0.1 M H$_2$SO$_4$ to achieve the pH between 6 and 8. After that, commercial H$_2$O$_2$ test solutions were added rapidly to the solution above. After 10 min (reaction time) at room temperature, the color of the resultant mixture solution changed

from colorless to orange as hydrogen peroxide reduced copper(II) ions to copper(I) ions in the presence of a phenanthroline derivative. Meanwhile, 2 mL of fresh electrolyte was added back to the cathode compartment to maintain electrolyte volume at 30 mL. Finally, the resultant mixture solution was filled into a standard 3.5 mL cuvette for UV−vis absorption spectra measurements. The absorbance value of the peak at 450 nm was recorded. The concentration−absorbance curves were calibrated using standard hydrogen peroxide solutions, including 0.016, 0.036, 0.055, and 0.076 mmol L^{-1} of H$_2$O$_2$.

Self-supported TiN/NF@Toray-irr GDEs were assembled in a single-compartment cell for electrochemistry studies such as CVs and LSVs and further in a two-compartment separated H-cell for H$_2$O$_2$ production and stability investigation. In the assembling cell, TiN/NF@Toray electrodes were in contact with the electrolyte (0.1 M KOH), and the GDE layer was in contact with air, which serves as O$_2$ supplier media. Subsequently, the CE was placed in the electrolyte section. The two electrodes were placed on opposite sides closely positioned to theAg/AgCl RE. Two 0.5 cm thick PTFE sheets with 0.2 cm wide by 0.8 cm long square sandwiched the catalyst layer, which served as interface with the liquid electrolyte. The geometric surface area of the catalyst was 0.16 cm^2.

Mechanistic insights were gained by carrying out electrochemical experiments in a conventional three-electrode system on various types of TiN NPs using a glassy carbon rotating disk electrode (RDE) and a rotating ring-disk electrode (RRDE) including a glassy carbon disk and a Pt ring as the second WE. All potentials were referred to the reversible hydrogen electrode (RHE). The catalyst ink was prepared by suspending the catalyst powder in a mixture containing Milli-Q water and Nafion solution (5 wt %, Sigma-Aldrich). After sonication, the catalyst ink was drop-casted onto the freshly polished glassy carbon electrode and dried at room temperature with humidity control.

RDEs (and RRDEs) were prepared by depositing 5 μL (10 μL) of ink with formulation catalyst/Nafion solution/H$_2$O = 3 mg/60 μL/940 μL. For preparing TiN-irr, the catalyst was peeled off from the surface of the TiN/NF@Toray-irr sample by sonication in H$_2$O and then used for the formulation of the ink. The potential was scanned between 0 and 1.2 V at 5 mV s^{-1}. Before LSV measurements, several CV sweeps from (1.2 to 0 V) at 20 mV s^{-1} were performed to stabilize the catalyst (usually, three cycles until a stable curve was achieved). Koutecky−Levich (K−L) plots were analyzed to calculate the number of electrons (n) transferred based on the K−L equation

$$\frac{1}{j} = \frac{1}{j_L} + \frac{1}{j_k} = \frac{1}{B\omega^{1/2}} + \frac{1}{j_k}$$

$$B = 0.62nFC_0(D_0)^{2/3}\nu^{-1/6}$$

where j_k is the kinetic current density, j is the measured current density, j_L is the diffusion limiting current density, ω is the angular frequency of rotation (rad s^{-1}), F is the Faraday constant (96,485 C mol^{-1}), C_0 is the bulk concentration of O$_2$ (1.26 × 10^{-3} mol L^{-1}), D_0 is the diffusion coefficient of O$_2$ in 0.1 M H$_2$SO$_4$ electrolyte (1.93 × 10^{-5} cm^2 s^{-1}), and the kinematic viscosity ν is 0.8926 × 10^{-2} cm^2 s^{-1} (at 25 °C).[68−71]

During RRDE measurements, the disk potential was scanned between 0 and 0.9 V vs RHE at a scan rate of 5 mV s^{-1} while the ring potential was fixed at 1.2 V vs RHE. The collection efficiency (N = 25.0%) of the RRDE was determined by using
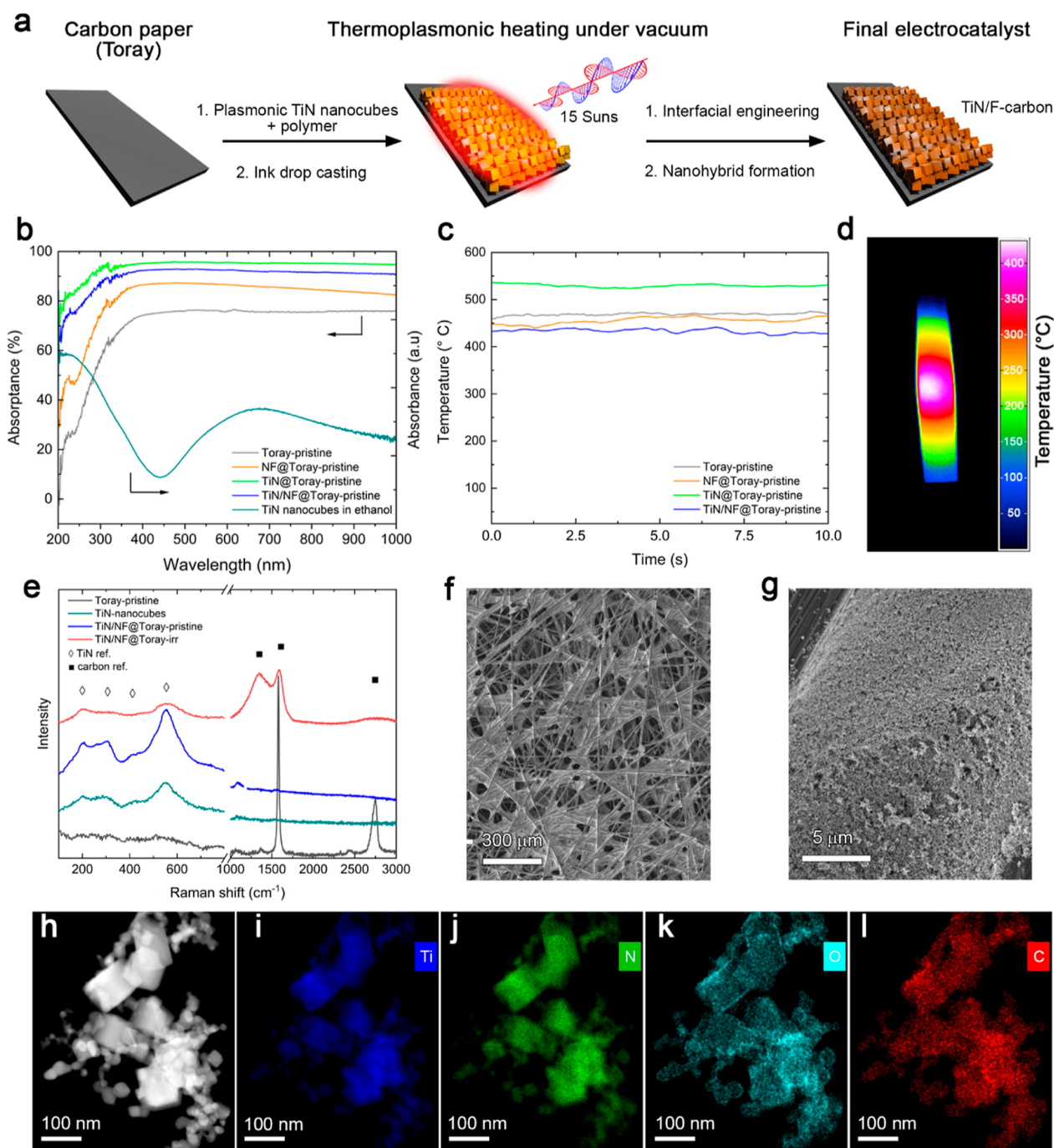
Figure 1. (a) Schematic of the thermoplasmonic fabrication strategy employed for the preparation of TiN/carbon nanohybrid electrodes. (b) Absorption spectra of TiN nanocubes in ethanol (dark green), Toray (gray), NF@Toray (yellow), TiN@Toray (green), and TiN/NF@Toray (blue) electrodes before irradiation. (c) Time-dependent steady-state temperatures under 15 suns irradiation of different samples measured using a thermal camera. (d) Thermal camera image of TiN/NF@Toray under 15 suns irradiation. (e) Raman spectra of Toray paper (black), TiN nanocubes (dark green), TiN/NF@Toray-pristine (blue), and TiN/NF@Toray-irr (red). (f,g) SEM images of TiN/NF@Toray-irr. (h) HAADF STEM micrograph and (i–l) EDS elemental mapping images of the electrocatalyst scratched from the top layer of TiN/NF@Toray-irr.

the $[Fe(CN)_6]^{3-}/[Fe(CN)_6]^{4-}$ system. H_2O_2 selectivity was calculated as follows

$$\text{selectivity}\,(H_2O_2) = 2 \times \frac{I_r/N}{I_r/N - I_d}$$

where I_d is the current detected at the disk and I_r is the current detected at the ring.

RESULTS AND DISCUSSION

Fabrication and Characterization of Hybrid Electrocatalysts. Mixing inorganic nanocrystals with polymers is an effective strategy to self-assemble them on a substrate forming very efficient broadband solar absorbers.[72] With this aim, we started the fabrication of our electrodes by forming inks containing plasmonic TiN nanocubes with 30 nm average size (Figure S2), and different ionomer binders dispersed in ethanol showing a localized surface plasmon peak at 650 nm (Figure S3).
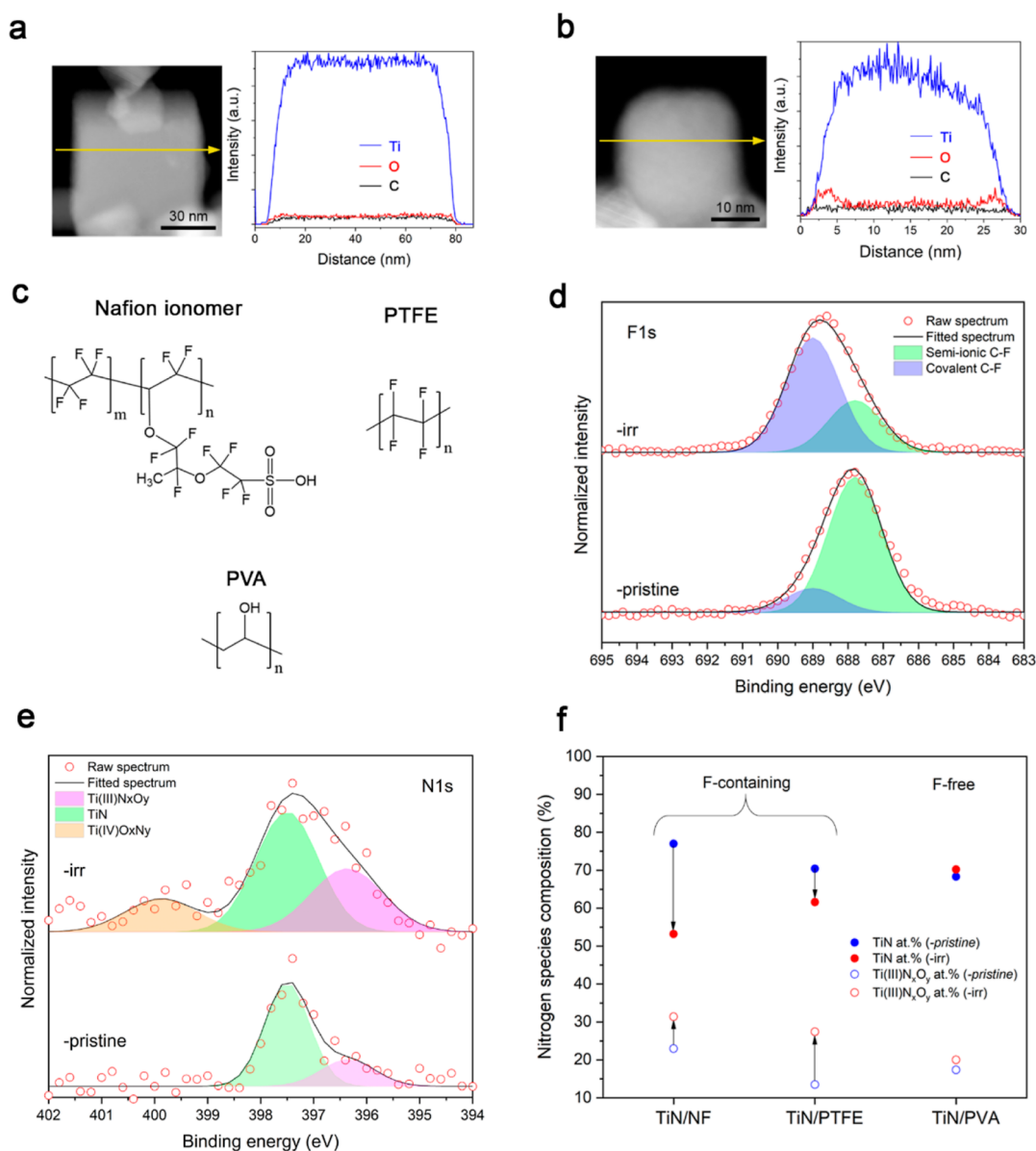
Figure 2. HAADF-STEM micrographs and EDS line scans of single TiN nanocubes from (a) TiN/NF@Toray-pristine and (b) TiN/NF@Toray-irr. (c) Chemical structure of the different polymeric binders used in the nanohybrids. HR-XPS spectra of TiN/NF@Toray-pristine and TiN/NF@Toray-irr in the region of (d) F 1s and (e) N 1s. (f) Comparison of N species content retrieved from the deconvoluted N1s spectra of the investigated samples before and after irradiation.

The synthetic procedure is schematically summarized in Figure 1a. Their subsequent drop-casting onto a porous carbon layer (i.e., Toray paper) produced TiN/binder nanocomposites absorbing above 90% of the incident light in the whole visible range (Figure 1b). To assess the generated photothermal heating (i.e., the thermoplasmonic effect), we excited samples at normal incidence, and an infrared (IR) camera was placed on the back of the films to detect temperature variations. Before acquiring the surface temperature, the spectral emissivity of the synthesized films was determined (Figure S4). The films containing plasmonic TiN nanocubes (TiN@Toray and TiN/NF@Toray) exhibited the highest optical absorption properties in the 300−1100 nm range (Figure 1b) and high photo-induced temperatures (Figure 1c) under 15 suns irradiation. The IR camera image of TiN/NF@Toray shows that there is a gradient of temperatures within the illuminated area, as the center reached 430 °C, while the lowest temperature of ∼300 °C was

detected at the periphery of the sample (Figure 1d). These conditions ensured the polymeric binder carbonization under vacuum. After photoirradiation for 2 h under vacuum, the as-synthesized hybrid films were obtained and named TiN/NF@Toray-irr. In contrast, the film before photoirradiation was named TiN/NF@Toray-pristine. A similar labeling was adopted for the films obtained with different organic binders.

The GIXRD patterns of the as-prepared films of the uncoated Toray paper and of the pristine TiN powder are shown in Figure S5. Pure Toray paper shows only one strong peak at $2\theta = 30.7°$ corresponding to the peak of pure graphite,[73,74] while both TiN/NF@Toray-pristine and Toray-irr show strong signal belonging to the Toray paper and the characteristic diffraction peaks of TiN.[75,76]

The Raman spectrum (Figure 1e) of TiN/NF@Toray-irr shows two broad peaks centered at 1350 and 1585 cm^{-1}, which can be attributed to the D and G bands, respectively, both bands

being absent in TiN/NF@Toray-pristine. The D band is associated with the sp^3 C bonds and defects, whereas the G band is related to sp^2 graphitic carbon.[77,78] Notably, this spectrum is significantly different from the one of Toray paper, which shows only a sharp peak at 1580 cm^{-1}. The additional peaks at ~423, 302, and 203 cm^{-1} and an intense peak at ~554 cm^{-1} were assigned to the crystalline TiN phase.[79−81] All these observations suggest that the thermoplasmonic heating induced the formation of new nanocarbon species deriving from the thermal decomposition of the organic binder, thus producing the formation of hybrid inorganic/organic nanocomposites.

The SEM images of TiN/NF@Toray-irr appear similar to the ones of the pristine sample and confirmed that the carbon fibers forming Toray paper are homogeneously covered with layers of TiN nanocubes self-assembled around them (Figures 1f,g and S6). The film made by closely packed TiN nanocubes can support multiple plasmonic resonance modes and produce electromagnetic hot spots in their contact areas that enable intense local heating and hot carrier generation.[82,83]

High-angle annular-dark-field scanning transmission electron microscopy (HAADF-STEM) and energy-dispersive X-ray spectroscopy (EDS) elemental maps of TiN/NF@Toray-irr reveal that Ti, N, and C are evenly distributed at the atomic level, suggesting the formation of TiN/carbon nanohybrids with homogeneous composition upon photoirradiation (Figure 1h−l). Notably, the same analysis performed on TiN nanocubes scraped off from TiN/NF@Toray-pristine shows no significant difference from the irradiated sample neither in particle size and morphology nor in elements distribution, which confirms that photoirradiation did not change the texture of the nano-composites (Figure S7). The only exception is for the O maps, which evidence a slightly more intense signal for TiN/NF@Toray-irr due to surface oxidation, as typically observed for TiN nanostructures exposed to air.[84] To better understand this observation, we performed a HAADF-STEM and EDX line scan analysis on single TiN nanocubes belonging both to TiN/NF@Toray-pristine and TiN/NF@Toray-irr (Figure 2a,b). In the latter, the EDS line of O highlights the presence of a thicker layer (~5 nm) at the surface of the TiN nanocube in comparison with the former, confirming the partial oxidation induced by the organic binder decomposition.

In order to gain insights into the surface chemical composition of the formed nanohybrids, we carried out XPS analysis of all investigated samples containing the following binders: NF, PTFE, and PVA, the latter taken as a reference containing no F species. All the chemical structures are shown in Figure 2c. The surface compositions extracted from the XPS survey spectra (Figure S8 and Table S1) highlight a significant increase of the carbon content and a decrease in Ti for all the films after irradiation. We also observed a significant reduction of both F (NF and PTFE) and O (PVA) content, suggesting the plasmonic-induced decomposition of the original molecular structure along with the in situ formation of new nanocarbons at the TiN surface. In detail, for samples containing NF, the overall relative amount of F species decreased ~10 at. % after irradiation. The same trend was observed for samples containing PTFE showing 4 at. % decrease of F species, while a stark decrease (~20 at. %) of O was revealed for TiN/PVA@Toray after irradiation, as expected from the decomposition of hydroxyl groups upon local heating.

The HR-XPS C1s spectra of TiN/NF@Toray-pristine and -irr (Figure S9a and Table S2) can be fitted with six peaks associated to C=C (284.8 eV), C−C (286.0 eV), C−O (287.2

eV), C=O (288.7 eV),[23,85] C−F (~289.8 eV), and C−F$_2$ (~291.6 eV).[30,86−88]

Notably, the overall relative amount of oxygenated functional groups increased by 1.5 at. % after irradiation, in agreement with the surface oxidation revealed by HRTEM EDS line scan analysis (Figure 2a). The same trend was observed for samples containing PTFE (Figure S10 and Table S3), while a stark decrease of O was revealed for TiN/PVA@Toray after irradiation, as expected from the decomposition of hydroxyl groups upon local heating (Figure S11a and Table S4).

The HR-XPS F1s spectra of TiN/NF@Toray (Figure 2d and Table S5) and TiN/PTFE@Toray (Figure S10b and Table S6) before and after irradiation could be fitted with two peaks: the first one centered at 688.3 eV was assigned to semi-ionic C−F species, while second one at 689.5 eV belonged to covalent C−F.[30,66,89] Notably, we observed for both samples after irradiation a drastic concentration decrease of the former and a stark increase of the latter, strongly indicating the plasmonic-induced in situ generation of F-doped nanocarbons.

The formation of fluorinated compounds may induce a change in the wettability of our Toray-based electrodes; therefore, we performed contact angle measurements on selected samples. Interestingly, the contact angle generated by a water droplet with TiN/NF@Toray-pristine and TiN/NF@Toray-irr was 129 and 139°, respectively (Figure S12). These results show a significantly increased hydrophobicity after the thermoplasmonic treatment, suggesting the formation of a superhydrophobic surface as an effect of F-doped nanocarbon formation. Similar contact angles were obtained in the state-of-the-art performing electrode after fluorination and were used to enhance the surface waterproofing performance[90,91] and improve oxygen transfer.[59,62−64]

To further explore the surface composition variation of the nanocomposites, we now focus the attention to the inorganic component (i.e., the TiN nanocubes).

On the one hand, the HR-XPS Ti2p spectra were deconvoluted using three peaks assigned to TiN, TiN$_x$O$_y$, and TiO$_2$ species, respectively.[81,84] The surface analysis of the samples containing fluorinated binders (Figures S9b, S10c and Tables S7, S8) shows a ~5 at. % increase of the TiO$_x$ phases (TiN$_x$O$_y$ and TiO$_2$ species) after illumination, while it remained constant for the samples with PVA (Figure S11b and Table S9).

On the other hand, the HR-XPS N 1s spectra for F-containing samples (Figures 2e and S10d and Tables S10 and S11) were fitted using three peaks, assigned to Ti$^{(III)}$N$_x$O$_y$ (~396.3 eV), TiN (~397.5 eV), and Ti$^{(IV)}$N$_x$O$_y$ (~399.8 eV), respectively.[39,92−97] Figure 2f reports the relative content of TiN and Ti$^{(III)}$N$_x$O$_y$ species retrieved from the spectra of pristine and irradiated samples. Interestingly, the TiN/F-binders (NF and PTFE)@Toray-irr show a 8−14 at.% increase in Ti$^{(III)}$N$_x$O$_y$ (corresponding to a 36−100% relative increase) concentration and a concomitant decrease in the TiN content. In contrast, the Ti$^{(III)}$N$_x$O$_y$ and TiN content remained nearly constant for TiN/PVA@Toray before and after irradiation (Figure S11c and Table S12). These results highlight that only the plasmonic-induced decomposition of F-containing binders promoted the recon-struction of the TiN nanocubes, favoring the formation of a surface layer richer in Ti$^{(III)}$N$_x$O$_y$.

Role of F-Containing Organic Binders on H$_2$O$_2$ Electrosynthesis. We first evaluated the performance of the prepared TiN/binder@Toray electrocatalysts in a conventional three-electrode cell. CV scans for TiN/NF@Toray-irr were carried out in Ar- and O$_2$-saturated 0.1 M KOH (Figure S13).
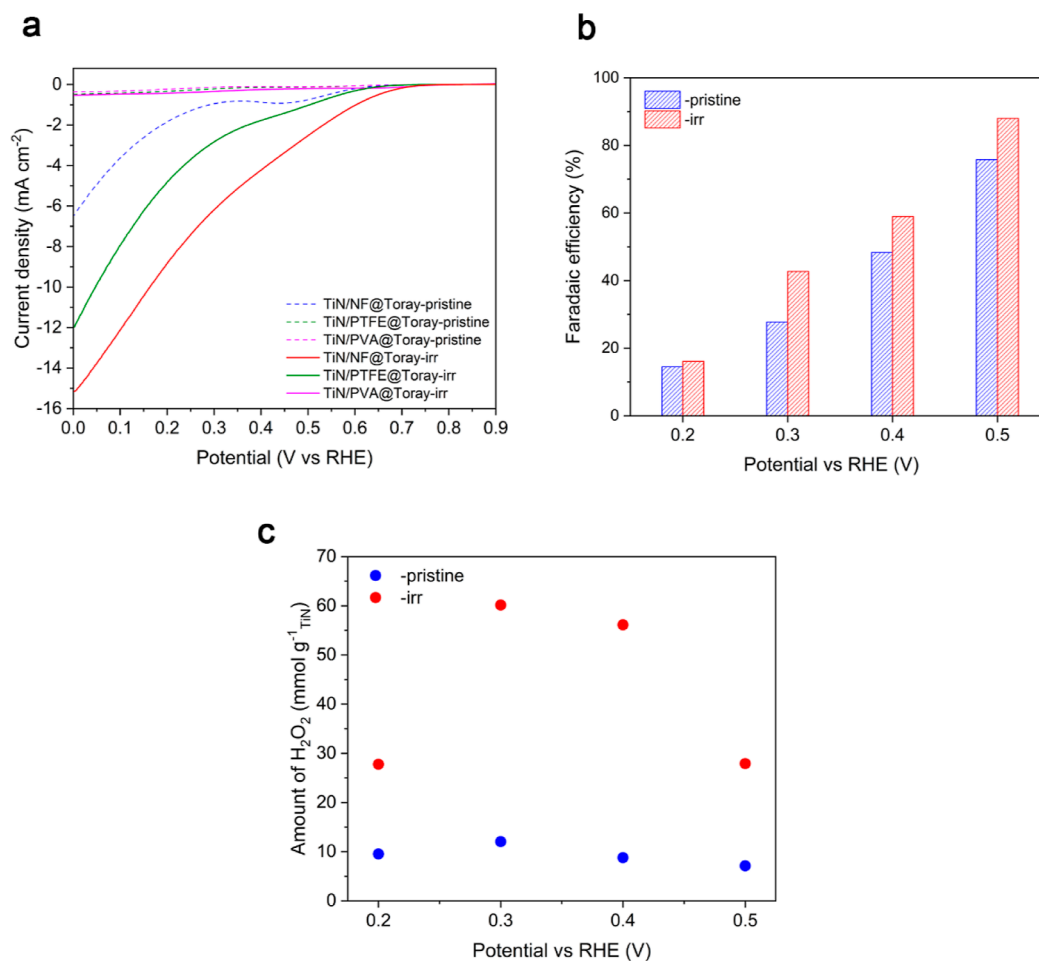
Figure 3. (a) LSV curves of investigated nanohybrid electrodes before and after irradiation obtained in a three-electrode cell. (b) FE and (c) H_2O_2 productivity for pristine and irradiated TiN/NF@Toray at different applied potentials using a H-cell configuration. All the measurements were performed in 0.1 M KOH saturated with O_2.

The enhanced current density observed in the presence of O_2 demonstrates that the main kinetic current is due to the ORR. The preparation of the TiN/binder@Toray electrocatalysts was optimized in terms of irradiation time (Figure S14) and TiN loading (Figure S15), finding that the highest performance was delivered for 2 h of irradiation using 1 mg of TiN.

Figure 3a shows the LSV curves of the investigated electrodes obtained using three different organic binders. Notably, the films containing the fluorinated binders exhibited a remarkable increase in ORR current after being irradiated, while TiN/PVA@Toray showed no ORR activity improvement. For instance, at 0.1 V vs RHE, TiN/PTFE@Toray shows a kinetic current density of 0.42 and 7.86 mA cm^{-2} before and after irradiation, respectively. Similarly, TiN/NF@Toray-irr displays a twice higher performance than TiN/NF@Toray-dark due to the reduced resistance to charge transfer at the solid/liquid interface, as demonstrated by electrochemical impedance spectroscopy measurements (Figure S16).

In order to recognize the contribution of each component forming the nanocomposite electrodes, films made by Toray, NF@Toray, and TiN@Toray were tested before and after irradiation. Figure S17a−c shows that no difference was recorded for neither TiN@Toray nor Toray samples. In contrast, NF@Toray-irr displayed a current density enhancement in comparison to NF@Toray-pristine, suggesting that the photoirradiation also in this case produced fluorinated nano-

carbons, which are active electrocatalysts for the ORR.[87,89,98] Furthermore, this current density comparison highlights that TiN/NF@Toray-irr shows up to 10 times higher current density at relevant applied potentials (see Figure S17d) than the films bearing only the individual components, remarking the crucial role played by the formation of the nanohybrid TiN/F-carbon@Toray electrocatalysts.

To confirm the uniqueness of the plasmon-induced fabrication approach, we prepared a reference TiN/NF@Toray electrocatalyst made by treating it under an inert gas atmosphere at 430 °C in a tubular furnace, replicating the same conditions obtained upon illumination. The LSV of this sample is very similar to the performance of TiN/NF@Toray-pristine (Figure S18), which suggests that both plasmonic local heating and generated hot carriers have a key role for obtaining a functional TiN surface reconstruction and active site formation.

Next, bulk electrolysis with the planar electrode was performed in a custom designed H-cell (Figure S19) by recording chronoamperometry curves (Figure S20) of TiN/NF@Toray at different applied potentials and monitoring the formation of H_2O_2 by a photometric method (see details in the Experimental Section). Figure 3b shows the calculated FE at four different applied bias for the sample before and after irradiation. The FE toward H_2O_2 increases from around 15−20% at 0.2 V vs RHE to 75−90% at 0.5 V vs RHE, where a remarkable FE as high as ∼90% for TiN/NF@Toray-irr was
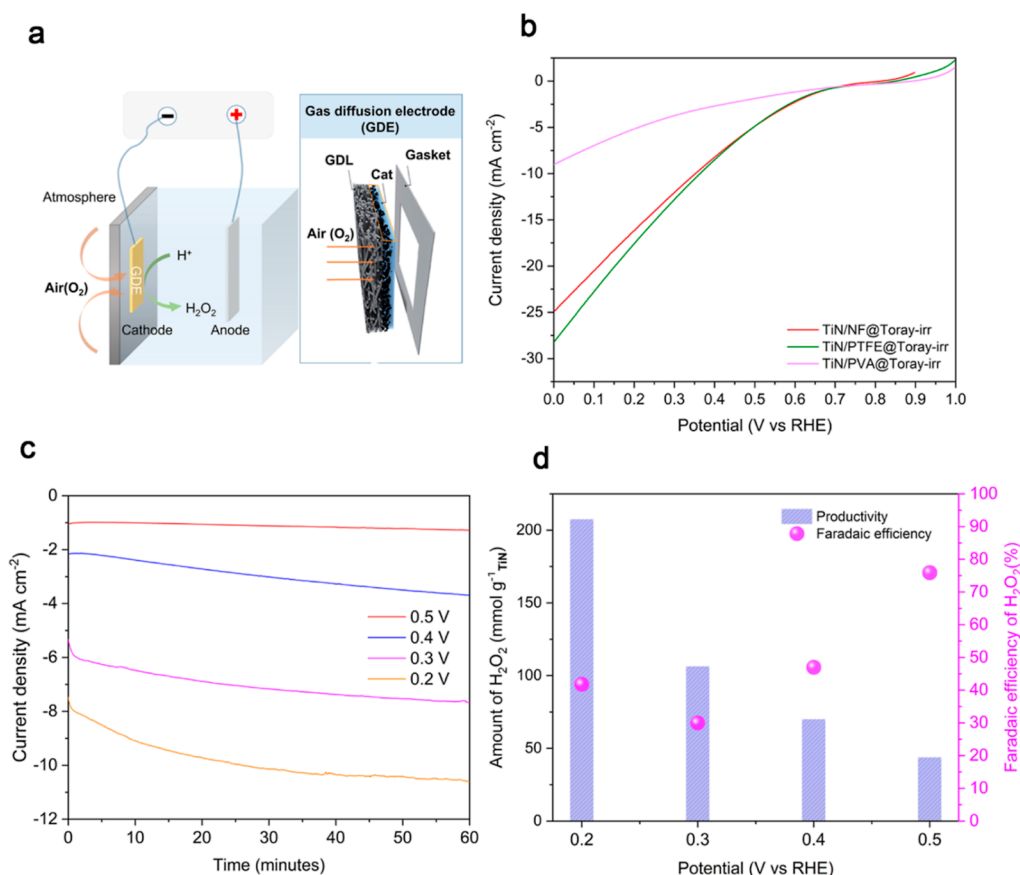
Figure 4. (a) Schematic of the GDE configuration with spontaneous air feeding. (b) Comparison of LSV curves of the electrodes containing the different organic binders after irradiation and tested using GDE configuration using a three-electrode cell in 0.1 M KOH. (c) Electrocatalytic performance of TiN/PTFE@Toray-irr in H-cell with GDEA: (c) chronoamperometry at different applied potentials and (d) corresponding FE and H_2O_2 productivity for TiN/PTFE@Toray-irr measured using a H-cell in 0.1 M KOH.

obtained. Notably, TiN/NF@Toray-irr always shows higher FE toward H_2O_2 than TiN/NF@Toray-pristine at any of the applied potentials explored. This trend is further highlighted in the H_2O_2 productivity plot (Figure 3c), which appears with a volcano shape reaching the maximum at 0.3 V vs RHE where the TiN/NF@Toray-irr reached ~60 mmol g_{TiN}^{-1} h^{-1} of H_2O_2 productivity, six times more than the pristine electrocatalyst.

Role of Ti$^{(III)}$N$_x$O$_y$ on the H_2O_2 Selectivity. To clarify how the surface Ti species influence the selectivity toward H_2O_2 formation, we performed RDE and RRDE experiments with electrocatalysts containing varying surface compositions. We compare pristine TiN nanocubes, TiN nanocubes treated at 800 °C for 2 h under ammonia (TiN−NH$_3$), and the powder scraped from TiN/NF@Toray-irr. The high-temperature treatment did not change the crystalline structure of TiN nanocubes (Figure S21) but allowed us to tune their surface compositions. In this way, we obtained a series of electrocatalysts featuring an increasing surface content of TiN (TiN−NH$_3$ > TiN nanocubes > TiN/NF@Toray-irr) and a concomitant decrease of Ti$^{(III)}$N$_x$O$_y$ concentration (TiN−NH$_3$ < TiN nanocubes < TiN/NF@Toray-irr), as retrieved from XPS measurements (Figure S22, Tables S13 and S14, referring to TiN/NF@Toray-irr Figures S9b, 2e and Tables S7 and S10).

From the LSV curves acquired using RDEs at different rotating speeds, we obtained K−L plots showing good linearity for all the investigated electrocatalysts (Figures S23−S25). Interestingly, the number of electrons characterizing the electrochemical process (n) shows that TiN/NF@Toray-irr

(i.e., the sample containing the lowest TiN and highest Ti$^{(III)}$N$_x$O$_y$ surface content) catalyzes the 2e$^-$ ORR (i.e., production of H_2O_2) in a significantly wider potential window (0.2−0.6 V vs RHE) in comparison with the sample having highest TiN and lowest Ti$^{(III)}$N$_x$O$_y$ content (TiN−NH$_3$) which was active only between 0.5 vs RHE and 0.6 V vs RHE. We also carried out RDE experiments of TiO$_2$ NPs showing that the oxide phase is able to drive ORR following the 2e$^-$ pathway in the same potential range (0.1−0.6 V vs RHE) but with much lower current density in comparison to TiN due to its insulating properties (Figure S26).

The RDE polarization curves discussed above show, for all samples, the presence of current maxima accompanied by only gradual current increase. This has been more or less confidently assigned by several authors to an ORR that proceeds under diffusion control or at least mixed diffusion-kinetic control regime.[99,100] The presence of such peaks gave rise to speculations about possible complex mechanistic steps: for example, the peaks could be associated to one-electron O_2 reduction to O_2^- which in alkaline solution can survive long enough to disproportionate and produce H_2O^-;[99,101] alternatively, mixed 2e$^-$ + 2e$^-$ and 4e$^-$ reduction processes have been hypothesized to lead to the formation of both H_2O_2 and H_2O.[100]

The selectivity trend observed in RDE measurements was confirmed by further electrocatalytic tests using the RRDE, which allowed us to assess electrochemically the H_2O_2 selectivity (Figure S27). In detail, TiN/NF@Toray-irr is the most selective electrocatalyst for H_2O_2 production, showing a

constant selectivity around 80% between 0.6 and 0.3 V vs RHE. Similar performances were recently observed in RRDE configuration for highly active O-and F-doped carbons creating an engineered reaction microenvironment for H_2O_2 electrosynthesis.[58] At lower potentials, the selectivity decreased reaching a still considerable 40% at 0.05 V vs RHE. TiN nanocubes showed a similar potential-dependent selectivity behavior but with lower performance in comparison of TiN/NF@Toray-irr. Otherwise, TiN−NH$_3$ shows a very low activity toward H_2O_2 synthesis, as evidenced by the 60% selectivity obtained only at 0.6 V vs RHE (where the kinetic current is at minimum values) and very rapidly decreasing to 5−10% already at 0.3 V vs RHE. These results highlight that the electrocatalyst featuring the highest $Ti^{(III)}N_xO_y$ surface content shows the highest H_2O_2 selectivity in a wider range of applied potentials. They also suggest that the performances of TiN-hybrid electrocatalysts are ensured on the one hand by the metallic conductivity of TiN (much higher than that of insulating TiO_2), while on the other hand, the passivated interface formed by $Ti^{(III)}N_xO_y/TiO_2$/F-nanocarbons is crucial to stir the ORR selectivity toward the $2e^-$ pathway, shifting the activity paradigm for metal nitrides that usually prefer the $4e^-$ mechanism.[27]

Electrochemical Testing with Natural Air Diffusion. Testing the films in a three-electrode configuration and completely immersing the Toray paper supporting the electrocatalysts in the electrolyte, we noted that their stability was limited, especially running bulk electrolysis at 0.2 V vs RHE of applied bias (i.e., when electrodes work at higher current densities) (Figure S20). This could be due to the flooding of the electrolyte through the Toray paper which produced a partial deactivation of the electrocatalysts.[102]

To solve this puzzle, we conducted ORR in a GDE configuration (Figure 4a), allowing natural air diffusion through the GDEs into the electrolyte and thus the spontaneous feeding oxygen to the cathode surface without the need for bubbling it into the electrolyte.

The LSV measurements carried out in this configuration show that the nanocomposites including the fluorinated nanocarbons achieved again the highest ORR current density, with TiN/PTFE@Toray-irr and TiN/NF@Toray-irr reaching ∼25 mA cm^{-2} at 0.1 V vs RHE (Figure 4b), while TiN/PVA@Toray-irr showing a much lower current (∼7 mA cm^{-2} at 0.1 V vs RHE), in agreement with the three-electrode cell tests. Importantly, bulk electrolysis with air GDEs performed in a custom designed H-cell (as shown in Figure S28) highlights the high stability of TiN/PTFE@Toray-irr even when high current density passes through the electrode (Figure 4c). This was further confirmed by the stability cycling test where the LSV curve obtained after 160 sweeps almost overlaps with the one obtained using the fresh electrode (Figure S29).

Notably, the natural air diffusion H-cell measurements with GDE made by TiN/PTFE@Toray-irr enabled to achieve a high H_2O_2 selectivity at 0.5 V vs RHE (∼80%) and an increased H_2O_2 productivity of 207 mmol g_{TiN}^{-1} h^{-1} at 0.2 V vs RHE with ∼40% H_2O_2 selectivity (Figure 4d). These values are 4−5 folds higher than that obtained in the conventional H-cell (Figure 3c) and could reach state-of-the art performances for carbon-based electrodes by engineering a custom-made flow cell.[58]

■ CONCLUSIONS

In summary, a TiN/F-doped nanocarbon hybrid was in situ prepared over GDE by local plasmonic heating. The electrode exhibited high stability, activity, and selectivity toward H_2O_2

formation during the ORR. Superior catalytic performances were achieved only when using F-containing polymers as binders, implying that the fluorination modification by both plasmonic heating and hot carriers played a crucial role in enhancing the activity of the nanohybrids. Mechanistic studies indicated that a surface enrichment in $Ti^{(III)}N_xO_y$ species obtained upon thermoplasmonic treatment determined an enhanced H_2O_2 selectivity. The in situ formed F-doped nanocarbons also provided superhydrophobic surface properties, thus enhancing the stability of the electrodes during operation at high current densities. Our methodology opens the way to large-scale manufacturing of superhydrophobic GDEs by surface plasmonic heating and can be implemented for a variety of energy- and industrially relevant electrochemical processes.

■ ASSOCIATED CONTENT

Ⓢ Supporting Information

The Supporting Information is available free of charge at https://pubs.acs.org/doi/10.1021/acscatal.3c01837.

Characterizations of materials and electrodes and electrochemical tests (PDF)

■ AUTHOR INFORMATION

Corresponding Author

Alberto Naldoni − *Department of Chemistry and NIS Centre, University of Turin, 10125 Turin, Italy;* ⓞ orcid.org/0000-0001-5932-2125; Email: alberto.naldoni@unito.it

Authors

Yu Zhang − *Czech Advanced Technology and Research Institute, Regional Centre of Advanced Technologies and Materials, Palacký University Olomouc, 78371 Olomouc, Czech Republic*

Luca Mascaretti − *Czech Advanced Technology and Research Institute, Regional Centre of Advanced Technologies and Materials, Palacký University Olomouc, 78371 Olomouc, Czech Republic;* ⓞ orcid.org/0000-0001-8997-7018

Michele Melchionna − *Department of Chemical and Pharmaceutical Sciences, ICCOM-CNR Trieste Research Unit, INSTM-Trieste, Center for Energy, Environment and Transport Giacomo Ciamician, University of Trieste, 34127 Trieste, Italy;* ⓞ orcid.org/0000-0001-9813-9753

Olivier Henrotte − *Czech Advanced Technology and Research Institute, Regional Centre of Advanced Technologies and Materials, Palacký University Olomouc, 78371 Olomouc, Czech Republic;* ⓞ orcid.org/0000-0002-7512-3377

Štepan Kment − *Czech Advanced Technology and Research Institute, Regional Centre of Advanced Technologies and Materials, Palacký University Olomouc, 78371 Olomouc, Czech Republic; Nanotechnology Centre, Centre of Energy and Environmental Technologies, VSB—Technical University of Ostrava, 708 00 Ostrava, Czech Republic;* ⓞ orcid.org/0000-0002-6381-5093

Paolo Fornasiero − *Department of Chemical and Pharmaceutical Sciences, ICCOM-CNR Trieste Research Unit, INSTM-Trieste, Center for Energy, Environment and Transport Giacomo Ciamician, University of Trieste, 34127 Trieste, Italy;* ⓞ orcid.org/0000-0003-1082-9157

Complete contact information is available at:
https://pubs.acs.org/10.1021/acscatal.3c01837

■ REFERENCES

(1) Govind Rajan, A.; Martirez, J. M. P.; Carter, E. A. Why Do We Use the Materials and Operating Conditions We Use for Heterogeneous (Photo)Electrochemical Water Splitting? *ACS Catal.* **2020**, *10*, 11177−11234.

(2) Yu, Z.-Y.; Duan, Y.; Feng, X.-Y.; Yu, X.; Gao, M.-R.; Yu, S.-H. Clean and Affordable Hydrogen Fuel from Alkaline Water Splitting: Past, Recent Progress, and Future Prospects. *Adv. Mater.* **2021**, *33*, 2007100.

(3) Seh, Z. W.; Kibsgaard, J.; Dickens, C. F.; Chorkendorff, I.; Nørskov, J. K.; Jaramillo, T. F. Combining theory and experiment in electrocatalysis: Insights into materials design. *Science* **2017**, *355*, No. eaad4998.

(4) Stephens, I. E. L.; Chan, K.; Bagger, A.; Boettcher, S. W.; Bonin, J.; Boutin, E.; Buckley, A. K.; Buonsanti, R.; Cave, E. R.; Chang, X.; et al. 2022 roadmap on low temperature electrochemical CO₂ reduction. *J. Phys. Energy* **2022**, *4*, 042003.

(5) Sun, Y.; Han, L.; Strasser, P. A comparative perspective of electrochemical and photochemical approaches for catalytic H2O2 production. *Chem. Soc. Rev.* **2020**, *49*, 6605−6631.

(6) Shi, X.; Back, S.; Gill, T. M.; Siahrostami, S.; Zheng, X. Electrochemical Synthesis of H2O2 by Two-Electron Water Oxidation Reaction. *Chem* **2021**, *7*, 38−63.

(7) Kirubakaran, A.; Jain, S.; Nema, R. K. A review on fuel cell technologies and power electronic interface. *Renewable Sustainable Energy Rev.* **2009**, *13*, 2430−2440.

(8) Fan, L.; Tu, Z.; Chan, S. H. Recent development of hydrogen and fuel cell technologies: A review. *Energy Rep.* **2021**, *7*, 8421−8446.

(9) Liu, Q.; Pan, Z.; Wang, E.; An, L.; Sun, G. Aqueous metal-air batteries: Fundamentals and applications. *Energy Storage Mater.* **2020**, *27*, 478−505.

(10) Li, M.; Bi, X.; Wang, R.; Li, Y.; Jiang, G.; Li, L.; Zhong, C.; Chen, Z.; Lu, J. Relating Catalysis between Fuel Cell and Metal-Air Batteries. *Matter* **2020**, *2*, 32−49.

(11) Jiang, Y.; Ni, P.; Chen, C.; Lu, Y.; Yang, P.; Kong, B.; Fisher, A.; Wang, X. Selective Electrochemical H2O2 Production through Two-Electron Oxygen Electrochemistry. *Adv. Energy Mater.* **2018**, *8*, 1801909.

(12) Hommura, S.; Kawahara, K.; Shimohira, T.; Teraoka, Y. Development of a Method for Clarifying the Perfluorosulfonated Membrane Degradation Mechanism in a Fuel Cell Environment. *J. Electrochem. Soc.* **2008**, *155*, A29.

(13) Brillas, E.; Alcaide, F.; Cabot, P.-L. s. A small-scale flow alkaline fuel cell for on-site production of hydrogen peroxide. *Electrochim. Acta* **2002**, *48*, 331−340.

(14) Yamanaka, I.; Onizawa, T.; Takenaka, S.; Otsuka, K. Direct and Continuous Production of Hydrogen Peroxide with 93 % Selectivity Using a Fuel-Cell System. *Angew. Chem., Int. Ed.* **2003**, *42*, 3653−3655.

(15) Yamanaka, I.; Hashimoto, T.; Ichihashi, R.; Otsuka, K. Direct synthesis of H2O2 acid solutions on carbon cathode prepared from activated carbon and vapor-growing-carbon-fiber by a H2/O2 fuel cell. *Electrochim. Acta* **2008**, *53*, 4824−4832.

(16) Yang, S.; Verdaguer-Casadevall, A.; Arnarson, L.; Silvioli, L.; Čolić, V.; Frydendal, R.; Rossmeisl, J.; Chorkendorff, I.; Stephens, I. E. L. Toward the Decentralized Electrochemical Production of H2O2: A Focus on the Catalysis. *ACS Catal.* **2018**, *8*, 4064−4081.

(17) Dong, K.; Liang, J.; Wang, Y.; Zhang, L.; Xu, Z.; Sun, S.; Luo, Y.; Li, T.; Liu, Q.; Li, N.; et al. Conductive Two-Dimensional Magnesium Metal−Organic Frameworks for High-Efficiency O2 Electroreduction to H2O2. *ACS Catal.* **2022**, *12*, 6092−6099.

(18) Du, J.; Jiang, S.; Zhang, R.; Wang, P.; Ma, C.; Zhao, R.; Cui, C.; Zhang, Y.; Kang, Y. Generation of Pd−O for Promoting Electro-chemical H2O2 Production. *ACS Catal.* **2023**, *13*, 6887−6892.

(19) Kodama, K.; Nagai, T.; Kuwaki, A.; Jinnouchi, R.; Morimoto, Y. Challenges in applying highly active Pt-based nanostructured catalysts for oxygen reduction reactions to fuel cell vehicles. *Nat. Nanotechnol.* **2021**, *16*, 140−147.

(20) Perazzolo, V.; Durante, C.; Pilot, R.; Paduano, A.; Zheng, J.; Rizzi, G. A.; Martucci, A.; Granozzi, G.; Gennaro, A. Nitrogen and sulfur doped mesoporous carbon as metal-free electrocatalysts for the in situ production of hydrogen peroxide. *Carbon* **2015**, *95*, 949−963.

(21) Lu, Z.; Chen, G.; Siahrostami, S.; Chen, Z.; Liu, K.; Xie, J.; Liao, L.; Wu, T.; Lin, D.; Liu, Y.; et al. High-efficiency oxygen reduction to hydrogen peroxide catalysed by oxidized carbon materials. *Nat. Catal.* **2018**, *1*, 156−162.

(22) Iglesias, D.; Giuliani, A.; Melchionna, M.; Marchesan, S.; Criado, A.; Nasi, L.; Bevilacqua, M.; Tavagnacco, C.; Vizza, F.; Prato, M.; et al. N-Doped Graphitized Carbon Nanohorns as a Forefront Electro-catalyst in Highly Selective O2 Reduction to H2O2. *Chem* **2018**, *4*, 106−123.

(23) Zhang, Y.; Melchionna, M.; Medved, M.; Błoński, P.; Steklý, T.; Bakandritsos, A.; Kment, Š.; Zbořil, R.; Otyepka, M.; Fornaserio, P.; et al. Enhanced On-Site Hydrogen Peroxide Electrosynthesis by a Selectively Carboxylated N-Doped Graphene Catalyst. *ChemCatChem* **2021**, *13*, 4372−4383.

(24) Dong, S.; Chen, X.; Zhang, X.; Cui, G. Nanostructured transition metal nitrides for energy storage and fuel cells. *Coord. Chem. Rev.* **2013**, *257*, 1946−1956.

(25) Cao, B.; Veith, G. M.; Diaz, R. E.; Liu, J.; Stach, E. A.; Adzic, R. R.; Khalifah, P. G. Cobalt Molybdenum Oxynitrides: Synthesis, Structural Characterization, and Catalytic Activity for the Oxygen Reduction Reaction. *Angew. Chem., Int. Ed.* **2013**, *52*, 10753−10757.

(26) Zhang, J.; Hu, H.; Liu, X.; Li, D. S. Development of the applications of titanium nitride in fuel cells. *Mater. Today Chem.* **2019**, *11*, 42−59.

(27) Zeng, R.; Yang, Y.; Feng, X.; Li, H.; Gibbs, L. M.; DiSalvo, F. J.; Abruña, H. D. Nonprecious transition metal nitrides as efficient oxygen reduction electrocatalysts for alkaline fuel cells. *Sci. Adv.* **2022**, *8*, No. eabj1584.

(28) Yang, N.; Zhu, X.; Wang, G.; Zhou, L.; Zhu, X.; Pan, J.; Yu, W.; Xia, C.; Tian, C. Pyrolysis-Free Mechanochemical Conversion of Small Organic Molecules into Metal-Free Heteroatom-Doped Mesoporous Carbons for Efficient Electrosynthesis of Hydrogen Peroxide. *ACS Mater. Lett.* **2023**, *5*, 379−387.

(29) Zeng, S.; Wang, S.; Zhuang, H.; Lu, B.; Li, C.; Wang, Y.; Wang, G. Fluorine-doped carbon: A metal-free electrocatalyst for oxygen reduction to peroxide. *Electrochim. Acta* **2022**, *420*, 140460.

(30) Chang, Y.; Chen, J.; Jia, J.; Hu, X.; Yang, H.; Jia, M.; Wen, Z. The fluorine-doped and defects engineered carbon nanosheets as advanced electrocatalysts for oxygen electroreduction. *Appl. Catal., B* **2021**, *284*, 119721.

(31) Jia, N.; Yang, T.; Shi, S.; Chen, X.; An, Z.; Chen, Y.; Yin, S.; Chen, P. N,F-Codoped Carbon Nanocages: An Efficient Electrocatalyst for Hydrogen Peroxide Electroproduction in Alkaline and Acidic Solutions. *ACS Sustainable Chem. Eng.* **2020**, *8*, 2883−2891.

(32) Patsalas, P.; Kalfagiannis, N.; Kassavetis, S.; Abadias, G.; Bellas, D. V.; Lekka, C.; Lidorikis, E. Conductive nitrides: Growth principles, optical and electronic properties, and their perspectives in photonics and plasmonics. *Mater. Sci. Eng., R* **2018**, *123*, 1−55.

(33) Li, W.; Guler, U.; Kinsey, N.; Naik, G. V.; Boltasseva, A.; Guan, J.; Shalaev, V. M.; Kildishev, A. V. Refractory Plasmonics with Titanium Nitride: Broadband Metamaterial Absorber. *Adv. Mater.* **2014**, *26*, 7959−7965.

(34) Krekeler, T.; Rout, S. S.; Krishnamurthy, G. V.; Störmer, M.; Arya, M.; Ganguly, A.; Sutherland, D. S.; Bozhevolnyi, S. I.; Ritter, M.; Pedersen, K.; et al. Unprecedented Thermal Stability of Plasmonic Titanium Nitride Films up to 1400 °C. *Adv. Opt. Mater.* **2021**, *9*, 2100323.

(35) Tian, X.; Luo, J.; Nan, H.; Fu, Z.; Zeng, J.; Liao, S. Binary transition metal nitrides with enhanced activity and durability for the oxygen reduction reaction. *J. Mater. Chem. A* **2015**, *3*, 16801−16809.

(36) Luo, J.; Tian, X.; Zeng, J.; Li, Y.; Song, H.; Liao, S. Limitations and Improvement Strategies for Early-Transition-Metal Nitrides as Competitive Catalysts toward the Oxygen Reduction Reaction. *ACS Catal.* **2016**, *6*, 6165−6174.

(37) Seifitokaldani, A.; Savadogo, O.; Perrier, M. Stability and catalytic activity of titanium oxy-nitride catalyst prepared by in-situ urea-based sol−gel method for the oxygen reduction reaction (ORR) in acid medium. *Int. J. Hydrogen Energy* **2015**, *40*, 10427−10438.

(38) Chisaka, M.; Ando, Y.; Itagaki, N. Activity and durability of the oxygen reduction reaction in a nitrogen-doped rutile-shell on TiN-core nanocatalysts synthesised via solution-phase combustion. *J. Mater. Chem. A* **2016**, *4*, 2501−2508.

(39) Chisaka, M.; Yamamoto, Y.; Itagaki, N.; Hattori, Y. Active Site Formation for Oxygen Reduction Reaction on Carbon-Support-Free Titanium Oxynitride with Boosted Activity in Acidic Media. *ACS Appl. Energy Mater.* **2018**, *1*, 211−219.

(40) Chisaka, M.; Xiang, R.; Maruyama, S.; Daiguji, H. Efficient Phosphorus Doping into the Surface Oxide Layers on TiN to Enhance Oxygen Reduction Reaction Activity in Acidic Media. *ACS Appl. Energy Mater.* **2020**, *3*, 9866−9876.

(41) Chisaka, M.; Ando, Y.; Yamamoto, Y.; Itagaki, N. A Carbon-Support-Free Titanium Oxynitride Catalyst for Proton Exchange Membrane Fuel Cell Cathodes. *Electrochim. Acta* **2016**, *214*, 165−172.

(42) Seifitokaldani, A.; Oishi, K.; Perrier, M.; Savadogo, O. Electrochemical and physicochemical properties of titanium Oxynitride electrocatalyst prepared by sol-gel methods for the oxygen reduction reaction purposes. *J. Solid State Electrochem.* **2015**, *19*, 3097−3109.

(43) Kreider, M. E.; Stevens, M. B.; Liu, Y.; Patel, A. M.; Statt, M. J.; Gibbons, B. M.; Gallo, A.; Ben-Naim, M.; Mehta, A.; Davis, R. C.; et al. Nitride or Oxynitride? Elucidating the Composition−Activity Relationships in Molybdenum Nitride Electrocatalysts for the Oxygen Reduction Reaction. *Chem. Mater.* **2020**, *32*, 2946−2960.

(44) Dong, K.; Liang, J.; Wang, Y.; Ren, Y.; Xu, Z.; Zhou, H.; Li, L.; Liu, Q.; Luo, Y.; Li, T.; et al. Plasma-induced defective TiO2-x with oxygen vacancies: A high-active and robust bifunctional catalyst toward H2O2 electrosynthesis. *Chem. Catal.* **2021**, *1*, 1437−1448.

(45) Naldoni, A.; Kudyshev, Z. A.; Mascaretti, L.; Sarmah, S. P.; Rej, S.; Froning, J. P.; Tomanec, O.; Yoo, J. E.; Wang, D.; Kment, Š.; et al. Solar Thermoplasmonic Nanofurnace for High-Temperature Heterogeneous Catalysis. *Nano Lett.* **2020**, *20*, 3663−3672.

(46) Guler, U.; Shalaev, V. M.; Boltasseva, A. Nanoparticle plasmonics: going practical with transition metal nitrides. *Mater. Today* **2015**, *18*, 227−237.

(47) Baffou, G.; Cichos, F.; Quidant, R. Applications and challenges of thermoplasmonics. *Nat. Mater.* **2020**, *19*, 946−958.

(48) Boyd, D. A.; Greengard, L.; Brongersma, M.; El-Naggar, M. Y.; Goodwin, D. G. Plasmon-Assisted Chemical Vapor Deposition. *Nano Lett.* **2006**, *6*, 2592−2597.

(49) Martino, G. D.; Michaelis, F. B.; Salmon, A. R.; Hofmann, S.; Baumberg, J. Controlling Nanowire Growth by Light. *Nano Lett.* **2015**, *15*, 7452−7457.

(50) Violi, I. L.; Gargiulo, J.; von Bilderling, C.; Cortés, E.; Stefani, F. D. Light-Induced Polarization-Directed Growth of Optically Printed Gold Nanoparticles. *Nano Lett.* **2016**, *16*, 6529−6533.

(51) Kamarudheen, R.; Kumari, G.; Baldi, A. Plasmon-driven synthesis of individual metal@semiconductor core@shell nanoparticles. *Nat. Commun.* **2020**, *11*, 3957.

(52) Mascaretti, L.; Schirato, A.; Zbořil, R.; Kment, Š.; Schmuki, P.; Alabastri, A.; Naldoni, A. Solar steam generation on scalable ultrathin thermoplasmonic TiN nanocavity arrays. *Nano Energy* **2021**, *83*, 105828.

(53) Cortés, E.; Xie, W.; Cambiasso, J.; Jermyn, A. S.; Sundararaman, R.; Narang, P.; Schlücker, S.; Maier, S. A. Plasmonic hot electron transport drives nano-localized chemistry. *Nat. Commun.* **2017**, *8*, 14880.

(54) Zhan, C.; Wang, Q.-X.; Yi, J.; Chen, L.; Wu, D.-Y.; Wang, Y.; Xie, Z.-X.; Moskovits, M.; Tian, Z.-Q. Plasmonic nanoreactors regulating selective oxidation by energetic electrons and nanoconfined thermal fields. *Sci. Adv.* **2021**, *7*, No. eabf0962.

(55) Mascaretti, L.; Schirato, A.; Fornasiero, P.; Boltasseva, A.; Shalaev, V. M.; Alabastri, A.; Naldoni, A. Challenges and prospects of plasmonic metasurfaces for photothermal catalysis. *Nanophotonics* **2022**, *11*, 3035−3056.

(56) Burdyny, T.; Smith, W. A. CO2 reduction on gas-diffusion electrodes and why catalytic performance must be assessed at commercially-relevant conditions. *Energy Environ. Sci.* **2019**, *12*, 1442−1453.

(57) Loukrakpam, R.; Ferreira Gomes, B.; Kottakkat, T.; Roth, C. A bird's eye perspective of the measurement of oxygen reduction reaction in gas diffusion electrode half-cell set-ups for Pt electrocatalysts in acidic media. *J. Phys. Mater.* **2021**, *4*, 044004.

(58) Xing, Z.; Shi, K.; Parsons, Z. S.; Feng, X. Interplay of Active Sites and Microenvironment in High-Rate Electrosynthesis of H2O2 on Doped Carbon. *ACS Catal.* **2023**, *13*, 2780−2789.

(59) Cao, P.; Quan, X.; Zhao, K.; Zhao, X.; Chen, S.; Yu, H. Durable and Selective Electrochemical H2O2 Synthesis under a Large Current Enabled by the Cathode with Highly Hydrophobic Three-Phase Architecture. *ACS Catal.* **2021**, *11*, 13797−13808.

(60) Chen, L.; Li, S.; Yang, Z.; Chen, C.; Chu, C.; Chen, B. Enhanced photocatalytic hydrogen peroxide production at a solid-liquid-air interface via microenvironment engineering. *Appl. Catal., B* **2022**, *305*, 121066.

(61) Panizza, M.; Cerisola, G. Electrochemical generation of H2O2 in low ionic strength media on gas diffusion cathode fed with air. *Electrochim. Acta* **2008**, *54*, 876−878.

(62) Van Nguyen, T.; Ahosseini, A.; Wang, X.; Yarlagadda, V.; Kwong, A.; Weber, A. Z.; Deevanhxay, P.; Tsushima, S.; Hirai, S. Hydrophobic Gas-Diffusion Media for Polymer-Electrolyte Fuel Cells by Direct Fluorination. *J. Electrochem. Soc.* **2015**, *162*, F1451−F1460.

(63) Yu, X.; Zhou, M.; Ren, G.; Ma, L. A novel dual gas diffusion electrodes system for efficient hydrogen peroxide generation used in electro-Fenton. *Chem. Eng. J.* **2015**, *263*, 92−100.

(64) Zhang, Q.; Zhou, M.; Ren, G.; Li, Y.; Li, Y.; Du, X. Highly efficient electrosynthesis of hydrogen peroxide on a superhydrophobic three-phase interface by natural air diffusion. *Nat. Commun.* **2020**, *11*, 1731.

(65) Zhang, Y.; Daniel, G.; Lanzalaco, S.; Isse, A. A.; Facchin, A.; Wang, A.; Brillas, E.; Durante, C.; Sirés, I. H2O2 production at gas-diffusion cathodes made from agarose-derived carbons with different textural properties for acebutolol degradation in chloride media. *J. Hazard. Mater.* **2022**, *423*, 127005.

(66) Kim, J.; Zhou, R.; Murakoshi, K.; Yasuda, S. Advantage of semi-ionic bonding in fluorine-doped carbon materials for the oxygen evolution reaction in alkaline media. *RSC Adv.* **2018**, *8*, 14152−14156.

(67) Xing, Z.; Hu, L.; Ripatti, D. S.; Hu, X.; Feng, X. Enhancing carbon dioxide gas-diffusion electrolysis by creating a hydrophobic catalyst microenvironment. *Nat. Commun.* **2021**, *12*, 136.

(68) Gubbins, K. E.; Walker, R. D. The Solubility and Diffusivity of Oxygen in Electrolytic Solutions. *J. Electrochem. Soc.* **1965**, *112*, 469.

(69) Itoe, R. N.; Wesson, G. D.; Kalu, E. E. Evaluation of Oxygen Transport Parameters in H[sub 2]SO[sub 4]-CH[sub 3]OH Mixtures Using Electrochemical Methods. *J. Electrochem. Soc.* **2000**, *147*, 2445.

(70) Wang, X.; Zhou, J.; Fu, H.; Li, W.; Fan, X.; Xin, G.; Zheng, J.; Li, X. MOF derived catalysts for electrochemical oxygen reduction. *J. Mater. Chem. A* **2014**, *2*, 14064−14070.

(71) Wang, Y. L.; Gurses, S.; Felvey, N.; Boubnov, A.; Mao, S. S.; Kronawitter, C. X. In Situ Deposition of Pd during Oxygen Reduction Yields Highly Selective and Active Electrocatalysts for Direct H2O2 Production. *ACS Catal.* **2019**, *9*, 8453−8463.

(72) Li, M.; Guler, U.; Li, Y.; Rea, A.; Tanyi, E. K.; Kim, Y.; Noginov, M. A.; Song, Y.; Boltasseva, A.; Shalaev, V. M.; et al. Plasmonic Biomimetic Nanocomposite with Spontaneous Subwavelength Structuring as Broadband Absorbers. *ACS Energy Lett.* **2018**, *3*, 1578−1583.

(73) Dobiášová, L.; Starý, V.; Glogar, P.; Valvoda, V. Analysis of carbon fibers and carbon composites by asymmetric X-ray diffraction technique. *Carbon* **1999**, *37*, 421−425.

(74) He, H.; Yang, F.; Ge, Y.; Ran, L.; Peng, K.; Yi, M. Effect of crystallinity of PAN-based carbon fiber surfaces on the formation characteristics of silicon carbide coating. *Mater. Res. Express* **2019**, *6*, 085603.

(75) Zhang, H.; Li, F.; Jia, Q. Preparation of titanium nitride ultrafine powders by sol−gel and microwave carbothermal reduction nitridation methods. *Ceram. Int.* **2009**, *35*, 1071−1075.

(76) Tang, S.; Cheng, Q.; Zhao, J.; Liang, J.; Liu, C.; Lan, Q.; Cao, Y.-C.; Liu, J. Preparation of Titanium nitride nanomaterials for electrode and application in energy storage. *Results Phys.* **2017**, *7*, 1198−1201.

(77) Hsu, C.-H.; Cloutier, S. G.; Palefsky, S.; Xu, J. Synthesis of Diamond Nanowires Using Atmospheric-Pressure Chemical Vapor Deposition. *Nano Lett.* **2010**, *10*, 3272−3276.

(78) Liu, Y.; Quan, X.; Fan, X.; Wang, H.; Chen, S. High-Yield Electrosynthesis of Hydrogen Peroxide from Oxygen Reduction by Hierarchically Porous Carbon. *Angew. Chem., Int. Ed.* **2015**, *54*, 6837−6841.

(79) Cheng, Y. H.; Tay, B. K.; Lau, S. P.; Kupfer, H.; Richter, F. Substrate bias dependence of Raman spectra for TiN films deposited by filtered cathodic vacuum arc. *J. Appl. Phys.* **2002**, *92*, 1845−1849.

(80) Saoula, N.; Djerourou, S.; Yahiaoui, K.; Henda, K.; Kesri, R.; Erasmus, R. M.; Comins, J. D. Study of the deposition of Ti/TiN multilayers by magnetron sputtering. *Surf. Interface Anal.* **2010**, *42*, 1176−1179.

(81) Hansen, K.; Cardona, M.; Dutta, A.; Yang, C. Plasma Enhanced Atomic Layer Deposition of Plasmonic TiN Ultrathin Films Using TDMATi and NH3. *Materials* **2020**, *13*, 1058.

(82) Govorov, A. O.; Zhang, W.; Skeini, T.; Richardson, H.; Lee, J.; Kotov, N. A. Gold nanoparticle ensembles as heaters and actuators: melting and collective plasmon resonances. *Nanoscale Res. Lett.* **2006**, *1*, 84.

(83) Baffou, G.; Berto, P.; Bermúdez Ureña, E.; Quidant, R.; Monneret, S.; Polleux, J.; Rigneault, H. Photoinduced Heating of Nanoparticle Arrays. *ACS Nano* **2013**, *7*, 6478−6488.

(84) Guler, U.; Zemlyanov, D.; Kim, J.; Wang, Z.; Chandrasekar, R.; Meng, X.; Stach, E.; Kildishev, A. V.; Shalaev, V. M.; Boltasseva, A. Plasmonic Titanium Nitride Nanostructures via Nitridation of Nanopatterned Titanium Dioxide. *Adv. Opt. Mater.* **2017**, *5*, 1600717.

(85) Reiche, S.; Blume, R.; Zhao, X. C.; Su, D.; Kunkes, E.; Behrens, M.; Schlögl, R. Reactivity of mesoporous carbon against water − An in-situ XPS study. *Carbon* **2014**, *77*, 175−183.

(86) Godet, C.; Sabbah, H.; Hervé, M.; Ababou-Girard, S.; Députier, S.; Perrin, A.; Guilloux-Viry, M.; Solal, F. Thermal stability of perfluorinated molecular monolayers immobilized on pulsed laser deposited amorphous carbon surfaces. *IOP Conf. Ser.: Mater. Sci. Eng.* **2010**, *16*, 012003.

(87) Panomsuwan, G.; Saito, N.; Ishizaki, T. Simple one-step synthesis of fluorine-doped carbon nanoparticles as potential alternative metal-free electrocatalysts for oxygen reduction reaction. *J. Mater. Chem. A* **2015**, *3*, 9972−9981.

(88) Jin, T.; Chen, J.; Wang, C.; Qian, Y.; Lu, L. Facile synthesis of fluorine-doped graphene aerogel with rich semi-ionic C−F bonds for high-performance supercapacitor application. *J. Mater. Sci.* **2020**, *55*, 12103−12113.

(89) Sun, X.; Zhang, Y.; Song, P.; Pan, J.; Zhuang, L.; Xu, W.; Xing, W. Fluorine-Doped Carbon Blacks: Highly Efficient Metal-Free Electrocatalysts for Oxygen Reduction Reaction. *ACS Catal.* **2013**, *3*, 1726−1729.

(90) Rabiee, H.; Ge, L.; Zhang, X.; Hu, S.; Li, M.; Yuan, Z. Gas diffusion electrodes (GDEs) for electrochemical reduction of carbon dioxide, carbon monoxide, and dinitrogen to value-added products: a review. *Energy Environ. Sci.* **2021**, *14*, 1959−2008.

(91) Pham, T. H. M.; Zhang, J.; Li, M.; Shen, T.-H.; Ko, Y.; Tileli, V.; Luo, W.; Züttel, A. Enhanced Electrocatalytic CO2 Reduction to C2+ Products by Adjusting the Local Reaction Environment with Polymer Binders. *Adv. Energy Mater.* **2022**, *12*, 2103663.

(92) Chan, M.-H.; Lu, F.-H. X-ray photoelectron spectroscopy analyses of titanium oxynitride films prepared by magnetron sputtering using air/Ar mixtures. *Thin Solid Films* **2009**, *517*, 5006−5009.

(93) Avasarala, B.; Haldar, P. Electrochemical oxidation behavior of titanium nitride based electrocatalysts under PEM fuel cell conditions. *Electrochim. Acta* **2010**, *55*, 9024−9034.

(94) Zgrabik, C. M.; Hu, E. L. Optimization of sputtered titanium nitride as a tunable metal for plasmonic applications. *Opt. Mater. Express* **2015**, *5*, 2786−2797.

(95) Jiang, S.; Yi, B.; Zhang, H.; Song, W.; Bai, Y.; Yu, H.; Shao, Z. Vertically Aligned Titanium Nitride Nanorod Arrays as Supports of Platinum−Palladium−Cobalt Catalysts for Thin-Film Proton Exchange Membrane Fuel Cell Electrodes. *ChemElectroChem* **2016**, *3*, 734−740.

(96) Chisaka, M. Creation of oxygen reduction reaction active sites on titanium oxynitride without increasing the nitrogen doping level. *Phys. Chem. Chem. Phys.* **2018**, *20*, 15613−15617.

(97) Chang, C.-C.; Nogan, J.; Yang, Z.-P.; Kort-Kamp, W. J. M.; Ross, W.; Luk, T. S.; Dalvit, D. A. R.; Azad, A. K.; Chen, H.-T. Highly Plasmonic Titanium Nitride by Room-Temperature Sputtering. *Sci. Rep.* **2019**, *9*, 15287.

(98) Zhao, K.; Su, Y.; Quan, X.; Liu, Y.; Chen, S.; Yu, H. Enhanced H2O2 production by selective electrochemical reduction of O2 on fluorine-doped hierarchically porous carbon. *J. Catal.* **2018**, *357*, 118−126.

(99) Wang, Y.; Zhang, D.; Liu, H. A study of the catalysis of cobalt hydroxide towards the oxygen reduction in alkaline media. *J. Power Sources* **2010**, *195*, 3135−3139.

(100) Szwabińska, K.; Lota, G. Mixed Diffusion-Kinetic Control of H2O2 Oxidation at an Oxide-Covered Platinum Electrode in Alkaline Electrolyte: Implications for Oxygen Electroreduction Studies with a Rotating Ring Disk Electrode. *ChemElectroChem* **2021**, *8*, 839−849.

(101) Kralj, S.; Longobardo, F.; Iglesias, D.; Bevilacqua, M.; Tavagnacco, C.; Criado, A.; Delgado Jaen, J. J.; Makovec, D.; Marchesan, S.; Melchionna, M.; et al. Ex-Solution Synthesis of Sub-5-nm FeOx Nanoparticles on Mesoporous Hollow N,O-Doped Carbon Nanoshells for Electrocatalytic Oxygen Reduction. *ACS Appl. Nano Mater.* **2019**, *2*, 6092−6097.

(102) Yang, K.; Kas, R.; Smith, W. A.; Burdyny, T. Role of the Carbon-Based Gas Diffusion Layer on Flooding in a Gas Diffusion Electrode Cell for Electrochemical CO2 Reduction. *ACS Energy Lett.* **2021**, *6*, 33−40.